CSI-EPT in Presence of RF-Shield for MR-Coils

CSI-EPT in presence of RF-shield for MR-coils

Authors

Alessandro Arduino[a,b]*, Luca Zilberti[b], Mario Chiampi[a], Oriano Bottauscio[b]

Author affiliation

[a] Dipartimento Energia – Politecnico di Torino – Corso Duca degli Abruzzi, 24 – 10129 Torino, Italia

[b] Istituto Nazionale di Ricerca Metrologica (INRIM) – Strada delle Cacce, 91 – 10135 Torino, Italia

* Correspondence should be addressed to: alessandro.arduino@polito.it

Published journal article available at DOI: https://doi.org/10.1109/TMI.2017.2665688

CSI-EPT in Presence of RF-Shield for MR-Coils

Alessandro Arduino, Luca Zilberti, Mario Chiampi, and Oriano Bottauscio, *Senior Member, IEEE*

***Abstract*—CSI-EPT is a recently developed technique for the electric properties tomography, that recovers the electric properties distribution starting from measurements performed by magnetic resonance imaging scanners. This method is an optimal control approach based on the contrast source inversion technique, which distinguishes itself from other electric properties tomography techniques for its capability to recover also the local specific absorption rate distribution, essential for online dosimetry. Up to now, CSI-EPT has only been described in terms of integral equations, limiting its applicability to homogeneous unbounded background. In order to extend the method to the presence of a shield in the domain—as in the recurring case of shielded radiofrequency coils—a more general formulation of CSI-EPT, based on a functional viewpoint, is introduced here. Two different implementations of CSI-EPT are proposed for a two-dimensional transverse magnetic model problem, one dealing with an unbounded domain and one taking into account the presence of a perfectly conductive shield. The two implementations are applied on the same virtual measurements obtained by numerically simulating a shielded radiofrequency coil. The results are compared in terms of both electric properties recovery and local specific absorption rate estimate, in order to investigate the requirement of an accurate modelling of the underlying physical problem.**

***Index Terms*—contrast source inversion, electric properties tomography, finite element method, magnetic resonance imaging, Maxwell equations, specific absorption rate**

I. Introduction

MAGNETIC resonance based electric properties tomography (MR-EPT) is a tomographic technique that aims at recovering the electric properties of a heterogeneous region starting from the measurements of radiofrequency (RF) magnetic fields performed by magnetic resonance imaging (MRI) scanners.

The increasing interest in MR-EPT is justified by numerous applications of the quantitative information it would give in addition to the traditional MRI results. For example, from a clinical oncology viewpoint MR-EPT would be a diagnostic tool, since it has been shown that some kinds of malign cancers have a higher electric conductivity with respect to the corresponding healthy tissue at the radiofrequency [1]–[3]. Furthermore, from the viewpoint of dosimetry, the knowledge of the electric properties is crucial for the estimation of local specific absorption rate (SAR), useful for example in hyperthermia therapy treatment planning [4], [5] and in MRI safety, where the presence of localised SAR hotspots could be dangerous [6], [7].

The possibility to perform the MR-EPT was originally mentioned by Haacke and collaborators in 1991 [8] and has been rediscovered in recent years with the proposal of a plethora of possible implementations [9]–[18]. The proposed techniques can be classified as local [9]–[13] and global [14]–[18] methods, depending on how much of the input data is used for the reconstruction of the electric properties in a certain point. Alternatively, it is possible to distinguish between direct [9]–[15] and inverse (or optimal control) [16]–[18] approaches, based on the underlying mathematics.

Among the implementations of MR-EPT that rely on optimal control theory, the contrast source inversion (CSI) MR-EPT [17] (in the paper it will be referred to as CSI-EPT) is of particular interest because of its capability to simultaneously recover both the electric property distributions and the electromagnetic field generated by the scanner in the examined body. This feature, in principle, makes the estimation of local SAR possible in real-time by simple algebraic manipulation of CSI-EPT results [19], [20]. When the electric properties have been recovered by other MR-EPT strategies, the electromagnetic field can be retrieved either by a simulation of the direct electromagnetic problem with the estimated properties, or by assuming a circularly polarized magnetic field and computing the electric field by the Ampère-Maxwell law. However, the former strategy can be extremely expensive from a computational viewpoint, whereas the latter can lead to inaccurate results when the contribution of neglected components is significant [19]. By virtue of this fact, CSI-EPT is a natural candidate for MRI safety applications.

Based on the well-known CSI technique for inverse scattering problems [21], the CSI-EPT procedure requires the solution of Maxwell equations in absence of the investigated object. Up to now, CSI-EPT has been described in terms of integral equations (IE) and tested on model problems in which virtual measurements are obtained from the numerical simulation of an unshielded RF coil [17], [19], [20]. However, a cylindrical shield is usually put around the coil in order to avoid the propagation of the RF field in the surrounding environment. In presence of such a shield, the current IE formulation of CSI-EPT would be very expensive, since it would require the numerical computation of Green's functions. In addition, the discretisation of the integral equation on a domain that is not rectangular—as may be in presence of a shield made of a perfect electric conductor (PEC)—may not lead to a discrete linear convolution and so reduces the efficiency of its evaluation by preventing the exploitation of the fast Fourier transform (FFT) algorithm [22].

Manuscript received July 20, 2016; revised XXX; accepted XXX. Date of publication XXX; date of current version XXX. *Asterisk indicates corresponding author*.

*A. Arduino is with the Dipartimento Energia, Politecnico di Torino, Italy and the Istituto Nazionale di Ricerca Metrologica (INRiM), Division of Metrology for Quality of Life, Torino, Italy (e-mail: alessandro.arduino@polito.it).

L. Zilberti and O. Bottauscio are with the Istituto Nazionale di Ricerca Metrologica (INRiM), Division of Metrology for Quality of Life, Torino, Italy (e-mail: l.zilberti@inrim.it and o.bottauscio@inrim.it).

M. Chiampi is with the Dipartimento Energia, Politecnico di Torino, Italy (e-mail: mario.chiampi@polito.it).

In order to overcome these issues, this paper presents a generalised formulation of the CSI-EPT method, based on a functional viewpoint and independent of the procedure adopted to solve Maxwell equations. The resulting technique is specialised for a two-dimensional transverse magnetic (TM) problem with the IE formulation for unbounded domains, recovering what was depicted in [17], and with a finite element method (FEM) formulation for bounded domains with PEC boundary. The FEM implementation of CSI-EPT recalls what was described in [23]. Finally, the two specialised techniques are applied to the same model problem in which virtual measurements are numerically obtained from the simulation of a whole-body birdcage coil with a PEC shield. In order to investigate the need for an accurate modelling of the underlying physical system to perform CSI-EPT, the results are compared in terms of electric properties reconstruction and local SAR estimation.

II. Generalised framework for CSI-EPT

A. Fundamental equations

The investigated body, whose properties are the electric conductivity σ, the electric permittivity ε, and the magnetic permeability μ_0—assumed equal to the one of vacuum as reasonable for biological tissues [24]—is immersed in a background with conductivity σ_b, permittivity ε_b, and permeability μ_0. Both the body and the background are linear and possibly heterogeneous. The RF coil of the scanner radiates the system with angular frequency ω. The electric properties are gathered in the complex permittivities $\tilde{\varepsilon} = \varepsilon - \mathrm{i}\sigma/\omega$ and $\tilde{\varepsilon}_\mathrm{b}$, by exploiting the time-harmonic domain assuming a factor $\mathrm{e}^{\mathrm{i}\omega t}$, omitted in the following.

The total electromagnetic field $\{\boldsymbol{E}, \boldsymbol{H}\}$ generated by the RF source is divided into the incident field $\{\boldsymbol{E}^\mathrm{i}, \boldsymbol{H}^\mathrm{i}\}$ produced by the same coil in absence of the investigated body, and the scattered field $\{\boldsymbol{E}^\mathrm{s}, \boldsymbol{H}^\mathrm{s}\} = \{\boldsymbol{E} - \boldsymbol{E}^\mathrm{i}, \boldsymbol{H} - \boldsymbol{H}^\mathrm{i}\}$, namely the distortion of the incident field due to the presence of the body. By subtracting the Maxwell equations for the total and the incident fields, the following equivalent equations for the scattered field are reached,

$$\begin{cases} \mathrm{curl}\ \boldsymbol{E}^\mathrm{s} = -\mathrm{i}\omega\mu_0\boldsymbol{H}^\mathrm{s}\,, & \text{in } \Omega \\ \mathrm{curl}\ \boldsymbol{H}^\mathrm{s} = \mathrm{i}\omega\tilde{\varepsilon}_\mathrm{b}\boldsymbol{E}^\mathrm{s} + \boldsymbol{J}^\mathrm{s}\,, & \text{in } \Omega \end{cases} \tag{1}$$

where Ω is the domain of interest, $\boldsymbol{J}^\mathrm{s} = \mathrm{i}\omega\tilde{\varepsilon}_\mathrm{b}\boldsymbol{w}$ is the equivalent scattering current, $\boldsymbol{w} = \chi\boldsymbol{E}$ is the contrast source of the scattering, and $\chi = \tilde{\varepsilon}/\tilde{\varepsilon}_\mathrm{b} - 1$ is the contrast of the object. By providing reasonable homogeneous boundary conditions on $\partial\Omega$ (or at infinity, in case of unbounded Ω), linear problem (1) admits one and only one solution $\{\boldsymbol{E}^\mathrm{s}, \boldsymbol{H}^\mathrm{s}\}$ with a continuous dependence on $\boldsymbol{w}$ [25], [26]. Equivalently, there exists a couple of bounded linear operators $\mathcal{S}_\mathrm{e}$ and $\mathcal{S}_\mathrm{h}$ such that

$$\boldsymbol{E}^\mathrm{s} = \mathcal{S}_\mathrm{e}\boldsymbol{w}\,, \qquad \boldsymbol{H}^\mathrm{s} = \mathcal{S}_\mathrm{h}\boldsymbol{w}\,. \tag{2}$$

By taking advantage of relations (2), both the contrast χ (the actual quantity to be evaluated in MR-EPT) and the contrast source $\boldsymbol{w}$ are treated as unknowns by the CSI-EPT method.

B. Cost functional

In the following it is assumed that both magnitude and phase of the transmit sensitivity B_1^+ of the RF coil are measured by the MRI scanner, being B_1^+ defined as

$$B_1^+ = \mu_0 \frac{H_x + \mathrm{i}H_y}{2}\,, \tag{3}$$

when the negative z-axis is directed as the static field B_0 [27]. Thus, defining the operator $\mathcal{P}$ such that for any vector field $\boldsymbol{u}$

$$\mathcal{P}\boldsymbol{u} = \frac{u_x + \mathrm{i}u_y}{2}\,, \tag{4}$$

and introducing the composed operator $\mathcal{S}_\mathrm{h}^+ = \mathcal{P}\mathcal{S}_\mathrm{h}$, for a generic guess $\boldsymbol{w}$ of the contrast source, the data residual $\rho[\boldsymbol{w}]$ results to be

$$\rho[\boldsymbol{w}] = B_1^{+;\mathrm{s}}/\mu_0 - \mathcal{O}\mathcal{S}_\mathrm{h}^+\boldsymbol{w}\,. \tag{5}$$

In (5) $B_1^{+;\mathrm{s}}$ is the scattered part of measured B_1^+, and $\mathcal{O}$ is the observation operator that mathematically models the measurement of the magnetic field.

On the other hand, since

$$\boldsymbol{w} = \chi\boldsymbol{E} = \chi\boldsymbol{E}^\mathrm{i} + \chi\boldsymbol{E}^\mathrm{s} = \chi\boldsymbol{E}^\mathrm{i} + \chi\mathcal{S}_\mathrm{e}\boldsymbol{w}\,, \tag{6}$$

the state residual $\boldsymbol{r}[\boldsymbol{w}, \chi]$ of the generic guess couple $(\boldsymbol{w}, \chi)$ is defined as

$$\boldsymbol{r}[\boldsymbol{w}, \chi] = \chi\boldsymbol{E}^\mathrm{i} + \chi\mathcal{S}_\mathrm{e}\boldsymbol{w} - \boldsymbol{w}\,, \tag{7}$$

where the incident field $\boldsymbol{E}^\mathrm{i}$ is an input for the problem. Both the electric and the magnetic incident fields, the latter being necessary to compute $B_1^{+;s}$, can be obtained either through an accurate numerical simulation of the antenna in free space, or by measurements of the incident electromagnetic field. In the latter case, the introduction of an additional specific observation operator for the state residual is required.

The CSI-EPT method recasts the inversion scattering problem as the minimisation of a cost functional, which combines the data and state errors,

$$F[\boldsymbol{w}, \chi] = \frac{\eta_\mathrm{d}}{2}\|\rho[\boldsymbol{w}]\|_\mathbb{D}^2 + \frac{\eta_\mathrm{s}[\chi]}{2}\|\boldsymbol{r}[\boldsymbol{w}, \chi]\|_\mathbb{S}^2\,, \tag{8}$$

where the weights $\eta_\mathrm{d} = \|B_1^{+;\mathrm{s}}/\mu_0\|_\mathbb{D}^{-2}$ and $\eta_\mathrm{s}[\chi] = \|\chi\boldsymbol{E}^\mathrm{i}\|_\mathbb{S}^{-2}$ appear, and the symbol $\|\cdot\|_\mathbb{X}$ denotes the norm on the linear space $\mathbb{X}$. Thus, $\mathbb{D}$ indicates the space of the data residual, that is related to the measurement domain, whereas $\mathbb{S}$ the space of the state residual. For the following computations it is convenient to work on Hilbert spaces $\mathbb{X}$ with inner product denoted by $(\cdot|\cdot)_\mathbb{X}$.

C. Minimisation procedure

In order to deal with the non-linearity of the problem, the minimisation is performed adopting a two-step alternating conjugate gradient method [17], [21].

The contrast source update step is performed with the iterative scheme

$$\boldsymbol{w}^{n+1} = \boldsymbol{w}^n + \alpha^n\boldsymbol{v}^n\,, \tag{9}$$

where α^n is a real constant step-length and $\boldsymbol{v}^n$ is the Polak–Ribière direction, described by

$$\begin{cases} \boldsymbol{v}^0 = \boldsymbol{0} \\ \boldsymbol{v}^n = \boldsymbol{g}^n + \dfrac{\left(\boldsymbol{g}^n | \boldsymbol{g}^n - \boldsymbol{g}^{n-1}\right)_{\mathbb{S}}}{\|\boldsymbol{g}^{n-1}\|_{\mathbb{S}}^2} \boldsymbol{v}^{n-1} \end{cases} \tag{10}$$

where $\boldsymbol{g}^n$ is the gradient of the cost functional F with respect to $\boldsymbol{w}$ evaluated at $(\boldsymbol{w}^n, \chi^n)$. Luckily, this gradient can be computed analytically by relying on Fréchet differential theory, to obtain (cf. Appendix)

$$\boldsymbol{g}^n = -\eta_{\mathrm{d}} \mathcal{S}_{\mathrm{h}}^{+;\star} \mathcal{O}^\star \rho^n - \eta_{\mathrm{s}}^n \left(\boldsymbol{r}^n - \mathcal{S}_{\mathrm{e}}^\star [\overline{\chi}^n \boldsymbol{r}^n] \right) , \tag{11}$$

where $\eta_{\mathrm{s}}^n = \eta_{\mathrm{s}}[\chi^n]$, $\rho^n = \rho[\boldsymbol{w}^n]$, $\boldsymbol{r}^n = \boldsymbol{r}[\boldsymbol{w}^n, \chi^n]$, the overbar represents the complex conjugation and the superscript star denotes the adjoint operators. Given the update direction $\boldsymbol{v}^n$, it is possible to choose the optimal step-length α^n analytically by solving the line minimisation problem, to obtain (cf. Appendix)

$$\alpha^n = \frac{-\left(\boldsymbol{g}^n | \boldsymbol{v}^n\right)_{\mathbb{S}}}{\eta_{\mathrm{d}} \|\mathcal{O} \mathcal{S}_{\mathrm{h}}^{+} \boldsymbol{v}^n\|_{\mathbb{D}}^2 + \eta_{\mathrm{s}}^n \|\chi^n \mathcal{S}_{\mathrm{e}} \boldsymbol{v}^n - \boldsymbol{v}^n\|_{\mathbb{S}}^2} . \tag{12}$$

The contrast update starts from the knowledge of the new contrast source $\boldsymbol{w}^{n+1}$. By assuming the weight η_{s}^n constant, the minimisation of the cost functional F with respect to the contrast χ consists in the minimisation of a convex functional, which can be analytically performed to obtain the update relation (cf. Appendix)

$$\chi^{n+1} = \frac{\boldsymbol{w}^{n+1} \cdot \overline{\left(\boldsymbol{E}^{\mathrm{i}} + \mathcal{S}_{\mathrm{e}} \boldsymbol{w}^{n+1}\right)}}{\left|\boldsymbol{E}^{\mathrm{i}} + \mathcal{S}_{\mathrm{e}} \boldsymbol{w}^{n+1}\right|^2} , \tag{13}$$

where the dot denotes the Euclidean scalar product between vectors, and the notation $|\cdot|$ indicates the vector length. Convex constraint of the contrast, as for example the positivity and negativity of respectively the real and imaginary part of χ, or the knowledge of null contrast in some regions, can be easily implemented by projection of the result of (13) after each iterative step [21].

In the following, the contrast source obtained by back propagation, namely the one that minimises the square of the norm of the data residual [21], is used as initial guess for the iterative procedure,

$$\boldsymbol{w}^1 = \frac{\|\mathcal{S}_{\mathrm{h}}^{+;\star} \mathcal{O}^\star B_1^{+;s}\|_{\mathbb{S}}^2}{\|\mathcal{O} \mathcal{S}_{\mathrm{h}}^{+} \mathcal{S}_{\mathrm{h}}^{+;\star} \mathcal{O}^\star B_1^{+;s}\|_{\mathbb{D}}^2} \mathcal{S}_{\mathrm{h}}^{+;\star} \mathcal{O}^\star B_1^{+;s} / \mu_0 . \tag{14}$$

Then, the starting contrast χ^1 is obtained by applying (13).

It is worth noting that the described minimisation scheme is absolutely general, since it is performed on the original functional spaces, with neither discretisations of the problem nor assumptions on the implementation of the operators.

III. Specific implementations

In this section two particular implementations of the CSI-EPT method are proposed. In both cases a two-dimensional TM problem in the xy-plane is considered, and the linear spaces are assumed to be $\mathbb{D} = \mathbb{C}^N$ and $\mathbb{S} = L^2(\Omega)$, with the inner products

$$(u|v)_{\mathbb{D}} = \mathrm{Re} \sum_{i=1}^{N} u_i \overline{v}_i , \quad \forall u, v \in \mathbb{D}, \tag{15}$$

$$(\boldsymbol{u}|\boldsymbol{v})_{\mathbb{S}} = \mathrm{Re} \int_\Omega \boldsymbol{u}(\boldsymbol{x}) \cdot \overline{\boldsymbol{v}}(\boldsymbol{x}) \mathrm{d}\boldsymbol{x} , \quad \forall \boldsymbol{u}, \boldsymbol{v} \in \mathbb{S} , \tag{16}$$

where Re denotes the real part.

Given an ordered collection of N points $(\boldsymbol{x}_i)_{i=1}^N$ where B_1^+ is measured, the observation operator is described for any scalar field u by the relation

$$\mathcal{O} u = \left(u(\boldsymbol{x}_i)\right)_{i=1}^N . \tag{17}$$

Consequently, the adjoint of the observation operator is such that for any N-dimensional vector $v = (v_i)_{i=1}^N$

$$\mathcal{O}^\star v = \sum_{i=1}^{N} v_i \delta_{\boldsymbol{x}_i} , \tag{18}$$

where $\delta_{\boldsymbol{x}_i}$ is the Dirac delta function centred in $\boldsymbol{x}_i$.

In addition, it is convenient to note that $\mathcal{S}_{\mathrm{h}}^{+;\star} = \mathcal{S}_{\mathrm{h}}^\star \mathcal{P}^\star$, where for any scalar field v

$$\mathcal{P}^\star v = \frac{v}{2} \left(\hat{x} - \mathrm{i}\hat{y}\right) , \tag{19}$$

with $\hat{x}$ and $\hat{y}$ the unit vectors directed as the x and y-axis, respectively.

A. Boundary-free domain

When the electromagnetic problem is defined on the whole space and Sommerfeld radiation conditions are imposed at infinity, problem (1) is analytically solved by the convolution of the dyadic Green's functions with the equivalent scattering current [26]. This is the case of an unshielded RF antenna in a homogeneous background. Precisely, relations (2) can be described by the same expressions detailed in [17]

$$\left(\mathcal{S}_{\mathrm{e}} \boldsymbol{w}\right)(\boldsymbol{x}) = \int_\Omega \left(\left(\nabla\nabla + k_{\mathrm{b}}^2 \mathcal{I} \right) \varphi(\boldsymbol{x} - \boldsymbol{y}) \right) \boldsymbol{w}(\boldsymbol{y}) \, \mathrm{d}\boldsymbol{y} , \tag{20}$$

and

$$\left(\mathcal{S}_{\mathrm{h}} \boldsymbol{w}\right)(\boldsymbol{x}) = \int_\Omega \mathrm{i}\omega \tilde{\varepsilon}_{\mathrm{b}} \nabla \varphi(\boldsymbol{x} - \boldsymbol{y}) \times \boldsymbol{w}(\boldsymbol{y}) \, \mathrm{d}\boldsymbol{y} , \tag{21}$$

where $\mathcal{I}$ is the identity operator, $k_{\mathrm{b}} = \omega \sqrt{\tilde{\varepsilon}_{\mathrm{b}} \mu_0}$ is the propagation coefficient of the radiation, and φ is the fundamental solution of the Helmholtz equation with propagation coefficient k_{b}—in two dimensions $\varphi(\boldsymbol{r}) = -\mathrm{i}H_0^{(2)}(k_{\mathrm{b}}|\boldsymbol{r}|)/4$, where $H_0^{(2)}$ is a Hankel function of the second kind, in three dimensions $\varphi(\boldsymbol{r}) = \exp(-\mathrm{i}k_{\mathrm{b}}|\boldsymbol{r}|)/(4\pi|\boldsymbol{r}|)$. Clearly, since the support of $\boldsymbol{w}$ is the bounded volume occupied by the investigated object, both integrals are well defined.

The adjoint of these operators are the correlation products of the conjugate transpose of the kernels with the input field

$$\left(\mathcal{S}_{\mathrm{e}}^\star \boldsymbol{v}\right)(\boldsymbol{x}) = \int_\Omega \left(\left(\nabla\nabla + \overline{k_{\mathrm{b}}^2} \mathcal{I} \right) \overline{\varphi}(\boldsymbol{y} - \boldsymbol{x}) \right) \boldsymbol{v}(\boldsymbol{y}) \, \mathrm{d}\boldsymbol{y} , \tag{22}$$

and

$$\left(\mathcal{S}_{\mathrm{h}}^\star \boldsymbol{v}\right)(\boldsymbol{x}) = \int_\Omega \mathrm{i}\omega \overline{\tilde{\varepsilon}_{\mathrm{b}}} \nabla \overline{\varphi}(\boldsymbol{y} - \boldsymbol{x}) \times \boldsymbol{v}(\boldsymbol{y}) \, \mathrm{d}\boldsymbol{y} , \tag{23}$$

for any vectorial field $\boldsymbol{v}$. If the domain is discretised with a uniform rectilinear grid, both primal and dual operators can be efficiently implemented by using the FFT algorithm [22], whose computational time is linearithmic. Specifically, for the following numerical tests the operators have been coded in C++ exploiting the efficiency of the library FFTW 3.3.4 [28] for FFT computations.

B. PEC shield

The mid-plane of a void shielded RF coil can be modelled by a two-dimensional TM cavity problem. In the following, the coil in presence of a body is approximated by the same model. In particular, assuming that the domain lies on the xy-plane, the electric field has only the z-component. Since PEC surface imposes the electric field to be perpendicular to the surface itself, problem (1) can be recast as the scalar problem with homogeneous Dirichlet boundary conditions for the electric field

$$\begin{cases} -\Delta E_z^{\mathrm{s}} - k_{\mathrm{b}}^2 E_z^{\mathrm{s}} = k_{\mathrm{b}}^2 w_z \,, & \text{in } \Omega \\ E_z^{\mathrm{s}} = 0 \,, & \text{on } \partial\Omega \end{cases} \tag{24}$$

where the domain Ω is the circle whose circumference $\partial\Omega$ is the PEC boundary. Thus, the operator $\mathcal{S}_{\mathrm{e}}$ is conveniently interpreted as the solver of problem (24).

Consequently, the result of applying the adjoint operator $\mathcal{S}_{\mathrm{e}}^{\star}$ to the generic scalar field v is obtained by multiplying by $\overline{k_{\mathrm{b}}^2}$ the solution of the adjoint problem [29]

$$\begin{cases} -\Delta u - \overline{k_{\mathrm{b}}^2} u = v \,, & \text{in } \Omega \\ u = 0 \,, & \text{on } \partial\Omega \end{cases} \tag{25}$$

Both the primal and the dual operators can be approximated by using any numerical method to solve the corresponding problem.

In the next numerical tests the solvers have been coded in C++ adopting linear FEM on a triangular mesh obtained by the open source software Triangle 1.6 [30]. Thus, problems (24) and (25) are approximated by linear systems whose coefficient matrices depend only on the background properties. Taking advantage of this fact, it is possible to reach a quadratic computational time for the single iterative step by factorising and storing the matrices only once for the whole procedure [23]. The library Eigen 3.2.8 [31] has been used for matrix manipulation.

By virtue of (1), the scattered magnetic field is obtained from E_z^{s} employing the differential operator $\mathcal{D}$ as follows,

$$\boldsymbol{H}^{\mathrm{s}} = \left(H_x^{\mathrm{s}}, H_y^{\mathrm{s}}\right) = \mathcal{D} E_z^{\mathrm{s}} = \frac{\mathrm{i}}{\omega\mu_0} \left(\frac{\partial E_z^{\mathrm{s}}}{\partial y}, -\frac{\partial E_z^{\mathrm{s}}}{\partial x} \right) . \tag{26}$$

Thus, the operator $\mathcal{S}_{\mathrm{h}}$ can be defined by composition as $\mathcal{D}\mathcal{S}_{\mathrm{e}}$, and its adjoint operator is $\mathcal{S}_{\mathrm{h}}^{\star} = \mathcal{S}_{\mathrm{e}}^{\star}\mathcal{D}^{\star}$, where

$$\mathcal{D}^{\star} \boldsymbol{v} = \frac{-\mathrm{i}}{\omega\mu_0} \left(\frac{\partial v_y}{\partial x} - \frac{\partial v_x}{\partial y} \right) \tag{27}$$

is the formal adjoint of $\mathcal{D}$ applied to any vector field $\boldsymbol{v}$.

The numerical implementation of $\mathcal{D}$ is trivial. Since the operator $\mathcal{S}_{\mathrm{e}}$ has been implemented by using linear FEM, its output is affine in each triangle of the mesh and $\mathcal{D}$ operates on it with an analitical output constant in each triangle. The numerical implementation of the dual operator $\mathcal{D}^{\star}$ is trickier, because it receives a piecewise constant input and should return a piecewise affine function. In order to approximate the value of $\mathcal{D}^{\star}\boldsymbol{v}$ on each node of the triangular mesh, in the following tests Stokes' theorem has been exploited. Precisely, with reference to Fig. 1, the following approximation has been used,

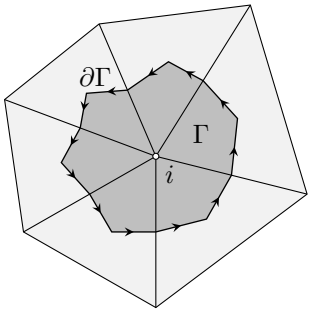

Fig. 1. Diagrammatic representation of the terms involved in (28). The path $\partial\Gamma$ connects the barycentre of each triangle with the one of its edges. The arrows show the direction of the tangent vector $\boldsymbol{\tau}$. The bounded region Γ is coloured with dark grey.

$$\left(\mathcal{D}^{\star}\boldsymbol{v}\right)_i \simeq \frac{1}{|\Gamma|} \int_{\Gamma} \mathcal{D}^{\star}\boldsymbol{v} \, \mathrm{d}S = \frac{-\mathrm{i}}{\omega\mu_0|\Gamma|} \oint_{\partial\Gamma} \boldsymbol{v} \cdot \boldsymbol{\tau} \, \mathrm{d}l \,. \tag{28}$$

The subscript i identifies the node in the mesh where the variable is evaluated, the curve $\partial\Gamma$ is obtained connecting the barycentre of each triangle with the barycentre of its edges, Γ is the bounded region of area $|\Gamma|$ delimited by $\partial\Gamma$, and $\boldsymbol{\tau}$ is the unit vector counterclockwise tangent to $\partial\Gamma$. The circuitation integral can be computed analitically for any piecewise constant vector field $\boldsymbol{v}$.

The particular implementation of the operators described in this chapter is one of the main novelty of this paper with respect to prior art.

IV. Numerical results and discussion

The mid-plane of a shielded whole-body volume coil has been modelled with TM assumption using 16 line sources located uniformly on a circle of radius 35.6 cm. The lines are driven by phase-shifted unitary currents at the Larmor frequency in order to generate an almost circular magnetic field in the inner region in absence of the investigated body. The antenna is surrounded by a concentric cylindrical PEC shield of radius 43.6 cm, representing the shield embedded in the scanner core. The electromagnetic field generated by this configuration in vacuum ($\varepsilon_{\mathrm{b}} = \varepsilon_0$, $\sigma_{\mathrm{b}} = 0$) has been assumed as the incident field and computed numerically using linear FEM on a triangular mesh.

A section of the abdomen of the anatomical human model Duke belonging to the Virtual Family [32] has been segmented with a resolution of 2 mm and placed inside the body-coil. The electric properties of the model tissues have been taken from the database of IT'IS Foundation [33], and are pictured in Fig. 2 at 128 MHz. The electromagnetic field generated by the line sources in presence of the body has

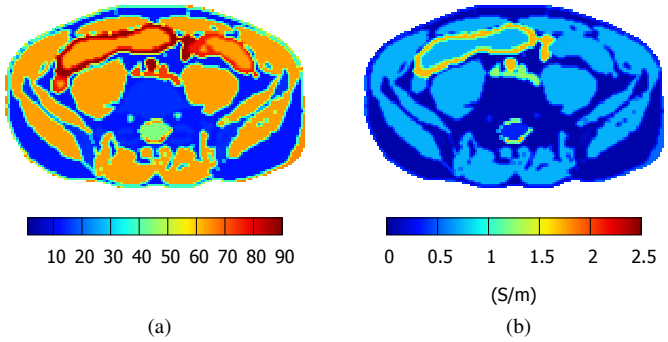

Fig. 2. Distribution of relative permittivity (a) and electric conductivity (b) in the considered section of the abdomen of the anatomical human model Duke at 128 MHz.

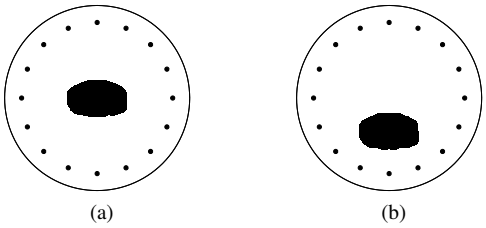

Fig. 3. Position of the body in the centre of the RF coil (a) and in the peripheral region of the domain (b).

been numerically computed. The transmit sensitivity B_1^+ of the resulting magnetic field has been evaluated on a Cartesian grid with 2 mm steps in the region occupied by the body and has been adopted as virtual noise-free measurements.

It is worth noting that the choice of the points of measurement can significantly affect the results of the inversion procedure. Not reported simulations show that, due to the abrupt change of properties between air and skin, information on the magnetic field at some points in air permits a better reconstruction of the electric properties with respect to the case where only measurements inside the investigated body are provided. Unfortunately, the latter situation is the one occurring when dealing with MRI scanners. In this case, the precision of the results can be restored by taking advantage of *a priori* knowledge, namely by imposing null contrast in air.

For the considered model problem, the natural implementation of CSI-EPT is the one described in Section III-B. Nonetheless, for the inverse problem also the implementation described in Section III-A has been used. In the following, the two approaches, referred to, respectively, as FEM-CSI and FFT-CSI, are applied to the model problem driven at 128 MHz, corresponding to a 3 T scanner. It must be noted that the faster FFT-CSI implementation quantifies the discrepancies on reconstructed electric properties and SAR by disregarding the presence of the shield.

The electric properties recovered by the two implementations after 5000 iterative steps when the investigated body is located in the middle of the coil (Fig. 3a) are pictured in Fig. 4. The maps of both electric properties are accurately reconstructed by FEM-CSI, whereas FFT-CSI shows an acceptable estimation of electric conductivity only. The plots of Fig. 5

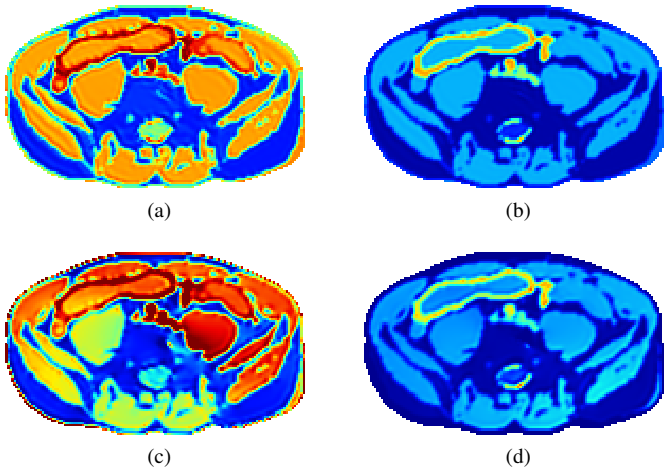

Fig. 4. Electric properties distributions recovered by FEM-CSI (a), (b) and FFT-CSI (c), (d) when Duke is located in the middle of the RF coil. Relative permittivity is reported in (a), (c), electric conductivity in (b), (d). Results at 128 MHz. The chromatic scales are the same as for Fig. 2.

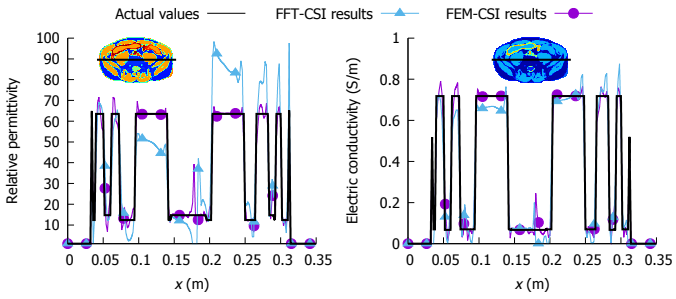

Fig. 5. Distributions of actual and reconstructed electric properties along the line depicted in the insets when Duke is located in the centre of the RF coil.

report the profile of the properties—actual and reconstructed—along the line depicted in the insets and allow a more quantitative analysis of the results. The errors introduced by FFT-CSI, which are larger in relative permittivity than in electric conductivity, are almost completely removed by FEM-CSI. Anyway, it is interesting to note that the interfaces between different tissues are precisely located by both implementations.

Fig. 6 reports the distributions of the electric properties recovered by both implementations after 5000 iterative steps when the examined body is translated in a peripheral region of the domain (Fig. 3b). The considered configuration is not representative of any real situation, but important to enhance the effect of the shield in close proximity of the human body and so to evaluate the method capabilities in a stressed situation. This time, FFT-CSI reconstructions are considerably wrong—the interactions between the equivalent scattering current and the PEC shield are stronger. On the other hand, FEM-CSI still estimates precisely the spatial distribution of the properties, except than for a small region where the total electric field reaches its minimum intensity. This known issue of CSI-EPT, which arises also in the most accurate FEM-CSI recovery, may be overcome by employing more than one measurement of the transmit sensitivity B_1^+, as suggested in [17].

More quantitatively, in Fig. 7 the boxplots, divided into

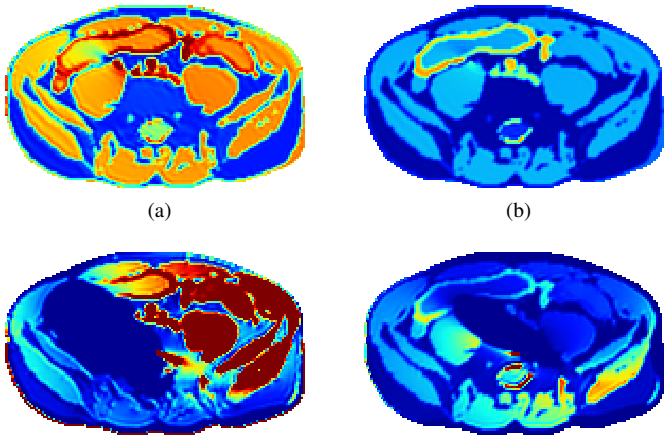

Fig. 6. Electric properties distributions recovered by FEM-CSI (a), (b) and FFT-CSI (c), (d) when Duke is located in a peripheral region of the domain. Relative permittivity is reported in (a), (c), electric conductivity in (b), (d). Results at 128 MHz. The chromatic scales are the same as for Fig. 2.

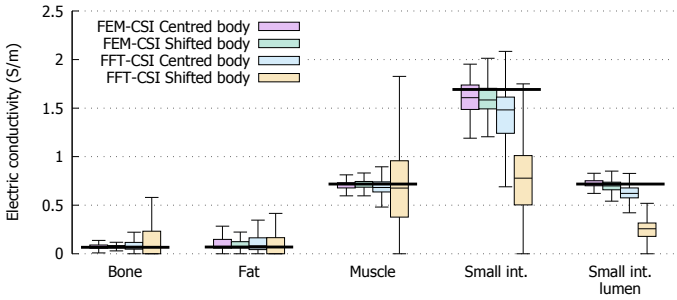

Fig. 7. Boxplots divided in quartiles of the electric conductivity at 128 MHz (3 T scanner) in some extended tissues. The black horizontal lines indicate the actual values.

quartiles, of the electric conductivity recovered by the two implementations for the two positionings are collected for some significant tissues. In each tissue, FEM-CSI leads to distributions with lower spatial variations than the ones of the FFT-CSI reconstructions. In addition, whereas the spatial variations of the distributions obtained by FEM-CSI are almost independent of the position of the investigated body, the variations of FFT-CSI distributions are generally higher when the body is in the periphery than when it is in the middle of the domain.

From an integral viewpoint, the behaviour of the two implementations is summarised in Fig. 8, where the value of the cost functional and the L^2 norm of the error in the contrast are reported step by step. The plots for FFT-CSI applied to the body placed in the peripheral region are not present, because they are out of range. Looking at the cost functional trend, it is possible to note that FFT-CSI reaches a minimum cost far away from zero, whereas FEM-CSI is monotonically decreasing independently of Duke's positioning. In addition, after some initial steps the cost of FEM-CSI remains lower when the body is in the peripheral region than when it is in the centre. This fact suggests that the closer the position of the body to the line sources, the lower the number of iterations needed to reach the same limit cost, confirming

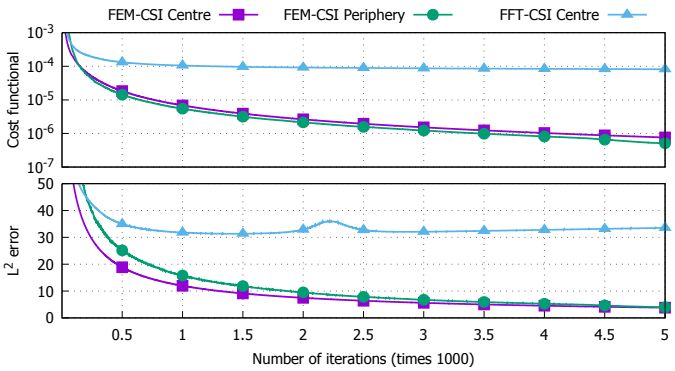

Fig. 8. Plot of the cost functional $F[\boldsymbol{w}, \chi]$ (above) and of the L^2 norm of the error in χ (below) against the number of iterations.

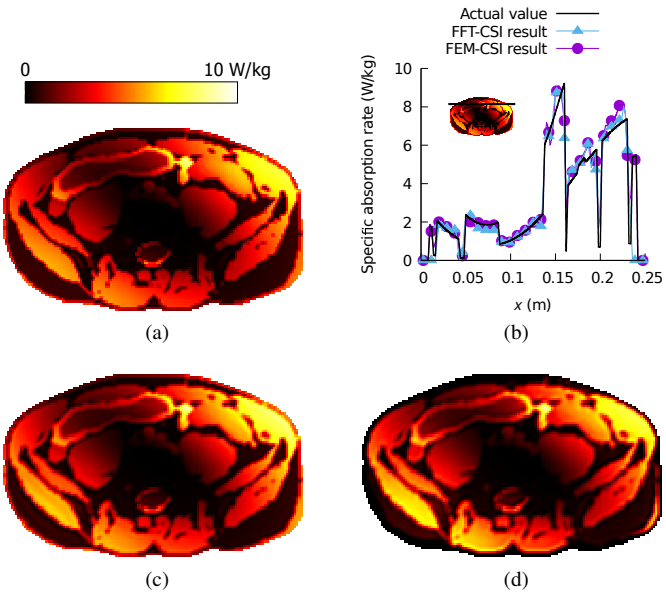

Fig. 9. Actual local SAR distribution in the worst-case SAR scenario when Duke is located in the centre of the RF coil (a). Actual and estimated local SAR along the line depicted in the inset (b). Local SAR distribution recovered by FEM-CSI (c) and FFT-CSI (d). Results at 128 MHz.

that, despite the homogeneity of the RF field used in MRI, strongly non-uniform input are in general convenient for MR-EPT. Analogous considerations can be deduced from the error, which tends to zero for FEM-CSI, but reaches a positive minimum for FFT-CSI. It is interesting to note that during the first 5000 iterative steps, in contrast with the previous observation about the cost functional, the global error is higher when the body is translated than when it is in the centre. Furthermore, whereas the minimisation procedure guarantees a monotonically decreasing trend of the cost functional, the same does not occur for the global error that can rise, as happens for FFT-CSI. These considerations recall that the cost functional is not a direct measure of the reconstruction error.

In Fig. 9, the estimations of the local SAR distributions are compared. By assuming that the density of the human body is uniform and equal to the one of water $\delta = 1000$ kg/m^3, the local SAR distribution can be easily estimated by the relation

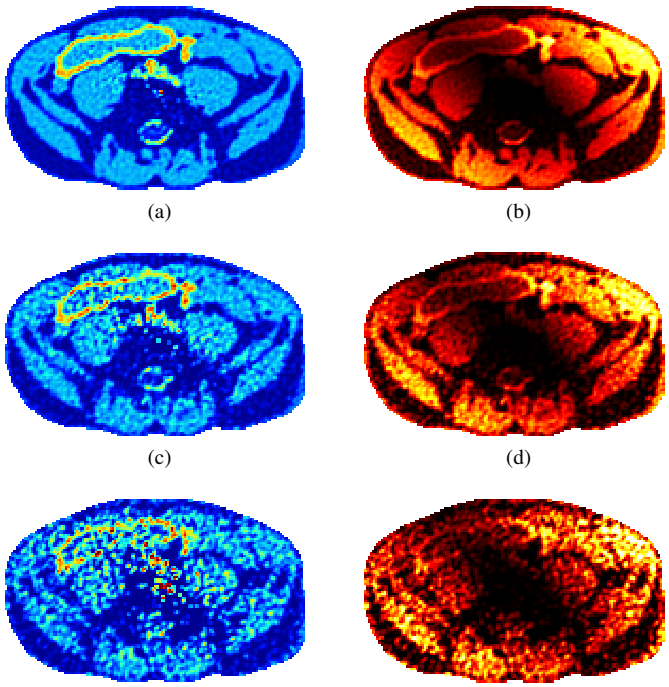

Fig. 10. Electric conductivity (a), (c), (e) and local SAR distribution (b), (d), (f) recovered by FEM-CSI from noisy input when Duke is in the centre of the RF coil driven at 128 MHz. Spatially uncorrelated noise is extracted in each point from a Gaussian distribution with null mean and standard deviation equal to 0.5% (SNR 200) (a), (b), 2% (SNR 50) (c), (d), and 5% (SNR 20) (e), (f) of the mean value of B_1^+. The chromatic scales are the same as in Fig. 2b for (a), (c), (e), and in Fig. 9 for (b), (d), (f).

$$\mathrm{SAR} = \frac{\sigma |\boldsymbol{E}|^2}{2\delta}\,, \tag{29}$$

where σ and $\boldsymbol{E} = \boldsymbol{E}^{\mathrm{i}} + \mathcal{S}_{\mathrm{e}}\boldsymbol{w}$ denote respectively the electric conductivity and the total electric field estimated by the CSI-EPT procedure. The resulting estimation of the local SAR can be used to check the compliance with safety regulations or guidelines [34], [35]. Actually, the value of the density of the human body is not completely known, showing in each tissue variations with respect to the density of water. The differences between FEM-CSI estimation and actual spatial distribution of the local SAR are mainly due to this fact. From this viewpoint, it should be preferable to talk about the volumetric dissipated power density instead of the local SAR in future revisions of the relevant standards.

The computed distributions are scaled to the worst-case SAR scenario, that is the configuration with global SAR estimated by the direct simulation equal to 2 W/kg. In the direct simulation, the maximum local SAR is equal to 9.24 W/kg and it is reached in the small intestine. Both the implementations accurately locate and estimate the maximum value—9.92 W/kg for FEM-CSI and 9.39 W/kg for FFT-CSI. In general, it can be stated that FFT-CSI estimation of the local SAR when Duke stays in the middle of the coil is satisfactory.

Lastly, some reconstructions of electric conductivity and estimations of local SAR from noisy input data are collected in Fig. 10, when Duke is located in the centre of the coil driven at 128 MHz. The noise associated to both real and imaginary part of the virtual measurement B_1^+ has been extracted in each measurement point according to a Gaussian distribution with null mean and standard deviation proportional to the mean value of B_1^+ inside the body. Thus, a spatially uncorrelated noise has been assumed. The proportionality factor has been chosen equal to 0.5%, 2%, and 5% based on the observation of some actual measurement of B_1^+ magnitude obtained by employing the Bloch-Siegert sequence on a 3 T scanner [36]. With reference to the definition of signal to noise ratio (SNR) given in [12], the considered noise extractions correspond to SNR 200, 50, and 20, respectively. In all the cases, the iterative process has been stopped after 5000 iterative steps. It appears clear that, in order to maintain a high quality reconstruction when the noise corrupting the input is high, additional regularisation strategies should be adopted, as the one suggested in [17], which can be reformulated in the general framework presented in this paper.

V. Conclusion

In this paper, a generalisation of CSI-EPT has been described adopting a functional viewpoint. By taking advantage of its generality, two different implementations have been proposed for a two-dimensional TM model problem: the FFT-CSI, that employs the dyadic Green's functions for Sommerfeld radiation conditions on homogeneous medium, and the FEM-CSI, that takes into account the presence of a PEC shield around the RF coil and applies also to heterogeneous background.

From a computational viewpoint, the code used for FFT-CSI is about ten times faster than the one written for FEM-CSI. Precisely, for the considered model problem, 1000 iterative steps require about 90 seconds in FFT-CSI and 950 seconds in FEM-CSI on an Intel Core i5 at 3.20 GHz. FFT-CSI is a preferable implementation since it can be easily efficiently coded and requires a computational domain a little larger than the investigated body. On the other hand, FEM-CSI forces to recover the electric properties on the whole domain, with a high number of discrete unknowns, and makes use of complex operators, which has been naïvely coded in current software. A possible improvement that would enhance FEM-CSI performances is, for example, the adoption of an adaptive mesh, which step by step reduces or increases the number of unknowns according to *a posteriori* error estimations of the solution at the previous iteration. In addition, both implementations would further benefit from parallel computing. The speed-up consequent to parallelisation is necessary in order to move towards realistic full-wave three-dimensional reconstructions, where, besides the longer computational times, also non-negligible memory consumption problems may arise.

Both implementations have been applied to virtual measurements obtained by simulating numerically a shielded whole-body coil in presence of a section of the abdomen of the anatomical human model Duke. FEM-CSI recovers precisely both electrical properties and estimates accurately the dissipated power density independently of the position of the investigated body. On the other hand, FFT-CSI, which

disregards the presence of the shield in the inverse procedure, introduces a sizeable error in the reconstruction of both electric properties and, consequently, in the estimation of local SAR. This result highlights that a precise modelling of the physical system is mandatory in order to perform quantitative imaging with CSI-EPT and justifies the introduction of the functional framework detailed in this paper.

Moreover, the proposed generalised formulation can be easily extended to include multiplicative regularisation and more than one measurement, as depicted in [17], as well as other variations to CSI like additive regularisation [37]. In addition, with reference to the functional formalism many numerical implementations can be easily adopted for CSI-EPT, like the ones relying on the finite difference method [38] or on the wavelet transform [39], in order to model the electromagnetic problem in the more realistic and efficient way and so reduce the errors in the reconstructions.

An issue that this paper overlooks is the so-called transceive phase assumption. Currently, only the transceive phase, namely the summation of the transmit and the receive phases, can be measured and the transmit phase is assumed to be equal to half of the measurement [40]. The transceive phase assumption validity worsen when the static field intensity rise, becoming an issue for ultra high field MRI, with Larmor frequencies above 128 MHz. For this reason, the possibility to include the transceive phase assumption directly in the CSI-EPT formulation should be further investigated.

APPENDIX

A. Computation of the gradient of the cost function with respect to the contrast source

The gradient $\boldsymbol{g}^n$ of the cost function (8) with respect to $\boldsymbol{w}$ can be easily computed as the limit value of the ratio of the differences [38]

$$\begin{aligned}(\boldsymbol{g}^n|\boldsymbol{u})_{\mathbb{S}} &= \lim_{h\to 0}\frac{F[\boldsymbol{w}^n+h\boldsymbol{u},\chi^n]-F[\boldsymbol{w}^n,\chi^n]}{h} = \\ &= \frac{\eta_{\mathrm{d}}}{2}\lim_{h\to 0}\frac{\|\rho[\boldsymbol{w}^n+h\boldsymbol{u}]\|_{\mathbb{D}}^2-\|\rho^n\|_{\mathbb{D}}^2}{h}+ \\ &+ \frac{\eta_{\mathrm{s}}^n}{2}\lim_{h\to 0}\frac{\|\boldsymbol{r}[\boldsymbol{w}^n+h\boldsymbol{u},\chi^n]\|_{\mathbb{S}}^2-\|\boldsymbol{r}^n\|_{\mathbb{S}}^2}{h}\,.\end{aligned} \tag{30}$$

Each limit can be performed independently. The first one, which is related to the data error, leads to

$$\begin{aligned}\lim_{h\to 0}\frac{h^2\|\mathcal{O}\mathcal{S}_{\mathrm{h}}^{+}\boldsymbol{u}\|_{\mathbb{D}}^2-2h\left(\rho^n|\mathcal{O}\mathcal{S}_{\mathrm{h}}^{+}\boldsymbol{u}\right)_{\mathbb{D}}}{h} &= \\ = -2\left(\mathcal{S}_{\mathrm{h}}^{+;\star}\mathcal{O}^{\star}\rho^n|\boldsymbol{u}\right)_{\mathbb{S}}\,,\end{aligned} \tag{31}$$

whereas the second one, related to the state error, leads to

$$\begin{aligned}\lim_{h\to 0}\frac{h^2\|\chi^n\mathcal{S}_{\mathrm{e}}\boldsymbol{u}-\boldsymbol{u}\|_{\mathbb{S}}^2+2h\left(\boldsymbol{r}^n|\chi\mathcal{S}_{\mathrm{e}}\boldsymbol{u}-\boldsymbol{u}\right)_{\mathbb{S}}}{h} &= \\ = 2\left(\mathcal{S}_{\mathrm{e}}^{\star}[\overline{\chi}^n\boldsymbol{r}^n]-\boldsymbol{r}^n|\boldsymbol{u}\right)_{\mathbb{S}}\,.\end{aligned} \tag{32}$$

Because of the generality of $\boldsymbol{u}\in\mathbb{S}$, these three relations can be combined to obtain (11).

B. Computation of the step-length

The optimal step-length α^n is the one that verifies the Euler equation

$$\frac{\mathrm{d}}{\mathrm{d}\alpha}F[\boldsymbol{w}^n+\alpha\boldsymbol{v}^n,\chi^n]\bigg|_{\alpha=\alpha^n}=0\,, \tag{33}$$

which can be treated using the chain-rule to obtain

$$(\boldsymbol{g}^n|\boldsymbol{v}^n)_{\mathbb{S}}+\alpha^n\left(\eta_{\mathrm{d}}\|\mathcal{O}\mathcal{S}_{\mathrm{h}}^{+}\boldsymbol{v}^n\|_{\mathbb{D}}^2+\eta_{\mathrm{s}}^n\|\chi^n\mathcal{S}_{\mathrm{e}}\boldsymbol{v}^n-\boldsymbol{v}^n\|_{\mathbb{S}}^2\right)=0\,, \tag{34}$$

whose solution leads to (12).

C. Contrast update formula

The contrast update formula is obtained minimising $\|\boldsymbol{r}[\boldsymbol{w}^{n+1},\chi]\|_{\mathbb{S}}^2$ with respect to χ. This operation is achieved by equating to zero the gradient computed with respect to χ of the objective,

$$\begin{aligned}\lim_{h\to 0}\frac{\|\boldsymbol{r}[\boldsymbol{w}^{n+1},\chi+hu]\|_{\mathbb{S}}^2-\|\boldsymbol{r}[\boldsymbol{w}^{n+1},\chi]\|_{\mathbb{S}}^2}{h} &= \\ -2\left(\boldsymbol{r}[\boldsymbol{w}^{n+1},\chi]|u\left(\mathcal{S}_{\mathrm{e}}\boldsymbol{w}^{n+1}+\boldsymbol{E}^{\mathrm{i}}\right)\right)_{\mathbb{S}} &= \\ 2\left(|\boldsymbol{E}^{\mathrm{i}}+\mathcal{S}_{\mathrm{e}}\boldsymbol{w}^{n+1}|^2\chi-\boldsymbol{w}^{n+1}\cdot\overline{(\boldsymbol{E}^{\mathrm{i}}+\mathcal{S}_{\mathrm{e}}\boldsymbol{w}^{n+1})}|\boldsymbol{u}\right)_{\mathbb{S}}&=0\,.\end{aligned} \tag{35}$$

The solution of this equation gives (13).

ACKNOWLEDGMENT

We thanks Dr. Gianluigi Tiberi for his useful contribution on noise quantification.

REFERENCES

[1] S. Y. Kim, J. Shin, D. H. Kim, M. J. Kim, E. K. Kim, H. J. Moon and J. H. Yoon, "Correlation between conductivity and prognostic factors in invasive breast cancer using magnetic resonance electric properties tomography (MREPT)," *Eur. Radiol.*, vol. 25, Oct. 2015.

[2] J. S. Shin, M. J. Kim, J. Lee, Y. Nam, M. Kim, N. Choi, S. Kim and D. H. Kim, "Initial study on in vivo conductivity mapping of breast cancer using MRI," *J. Magn. Reson.* Imag., vol. 42, no. 2, pp. 371-378, Aug. 2015.

[3] M. Lazebnik, D. Popovic, L. McCartney, C. B. Watkins, M. J. Lindstrom, J. Harter, S. Sewall, T. Ogilvie, A. Magliocco, T. M. Breslin, W. Temple, D. Mew, J. H. Booske, M. Okoniewski and S. C. Hagness, "A large-scale study of the ultrawideband microwave dielectric properties of normal, benign and malignant breast tissues obtained from cancer surgeries," *Phys. Med. Biol.*, vol. 52, no. 20, pp. 6093-6115, Oct. 2007.

[4] H. P. Kok, P. Wust, P. R. Stauffer, F. Bardati, G. C. Van Rhoon and J. Crezee, "Current state of the art of regional hyperthermia treatment planning: a review," *Radiat. Oncol.*, vol. 10, no. 1, Sep. 2015.

[5] E. Balidemaj, H. P. Kok, G. Schooneveldt, A. L. H. M. W. Van Lier, R. F. Remis, L. J. A. Stalpers, H. Westerveld, A. J. Nederveen, C. A. T. Van den Berg and J. Crezee, "Hyperthermia treatment planning for cervical cancer patients based on electrical conductivity tissue properties acquired in vivo with EPT at 3 T MRI," *Int. J. Hyperthermia*, Mar. 2016.

[6] G. Tiberi, N. Fontana, M. Costagli, R. Stara, L. Biagi, M.R. Symms, A. Monorchio, A. Retico, M. Cosottini, and M. Tosetti, "Investigation of maximum local specific absorption rate in 7 T magnetic resonance with respect to load size by use of electromagnetic simulations," *Bioelectromagnetism*, vol. 36, no. 5, pp. 358-366, Jul. 2015.

[7] M.C. Restivo, C.A.T. van den Berg, A.L.H.M.W. van Lier, D.L. Polders, A.J.E. Raaijmakers, P.R. Luijten, and H. Hoogduin, "Local specific absorption rate in brain tumors at 7 Tesla," *Magn. Reson. Med.*, vol. 75, no. 1, pp. 381-389, Jan. 2016.

[8] E.M. Haacke, L.S. Pepropoulos, E.W. Nilges, and D.H. Wu, "Extraction of conductivity and permittivity using magnetic resonance imaging," *Phys. Med. Biol.*, vol. 36, no. 6, pp. 723-734, 1991.

[9] U. Katscher, T. Voigt, C. Findeklee, P. Vernickel, K. Nehrke, and O. Doessel, "Determination of electric conductivity and local SAR via B1 mapping," *IEEE Trans. Med. Imag.*, vol. 28, no. 9, pp. 1365-1374, Sep. 2009.

[10] T. Voigt, U. Katscher and O. Doessel, "Quantitative conductivity and permittivity imaging of the human brain using electric properties tomography," *Magn. Reson. Med.*, vol. 66, no. 2, pp. 456-466, Aug. 2011.

[11] J. Lee, J. Shin, and D. H. Kim, "MR-based conductivity imaging using multiple receiver coils," *Magn. Reson. Med.*, vol. 76, no. 2, pp. 530-539, Aug. 2016.

[12] X. Zhang, S. Zhu and B. He, "Imaging electric properties of biological tissues by RF field mapping in MRI," *IEEE Trans. Med. Imag.*, vol. 29, no. 2, pp. 474-481, Feb. 2010.

[13] J. Liu, X. Zhang, S. Schmitter, P.F. Van de Moortele and B. He, "A robust method for mapping electrical properties of biological tissues in vivo using magnetic resonance imaging," *Magn. Reson. Med.*, vol. 74, no. 3, pp. 634-646, Sep. 2015.

[14] F. S. Hafalir, O. F. Oran, N. Gurler and Y. Z. Ides, "Convection-reaction equation based magnetic resonance electrical properties tomography (cr-MREPT)," *IEEE Trans. Med. Imag.*, vol. 33, no. 3, pp. 777-793, Mar. 2014.

[15] R. Schmidt and A. Webb, "A new approach for electrical properties estimation using a global integral equation and improvements using high permittivity materials," *J. Magn. Reson.*, vol. 262, pp. 8-14, Jan. 2016.

[16] H. Ammari, H. Kwon, Y. Lee, K. Kang and J. K. Seo, "Magnetic resonance-based reconstruction method of conductivity and permittivity distributions at the Larmor frequency," *Inv. Probl.*, vol. 31, no. 10, pp. 105001-105024, Sep. 2015.

[17] E. Balidemaj, C. A. T. Van den Berg, J. Trinks, A. L. H. M. W. Van Lier, A. J. Nederveen, L. J. A. Stalpers, H. Crezee and R. F. Remis, "CSI-EPT: a contrast source inversion approach for improved MRI-based electric properties tomography," *IEEE Trans. Med. Imag.*, vol. 34, no. 9, pp. 1788-1796, Sep. 2015.

[18] A. Borsic, I Perreard, A. Mahara and R. J. Halter, "An inverse problems approach to MR-EPT image reconstruction," *IEEE Trans. Med. Imag.*, vol. 35, no. 1, pp. 244-256, Jan. 2016.

[19] A. Arduino, M. Chiampi, L. Zilberti and O. Bottauscio, "Alternative approaches to magnetic resonance-based electric properties tomography and local specific absorption rate estimation," *IEEE Trans. Magn.*, vol. 53, no. 2, Feb. 2017, Art. no. 5100108.

[20] E. Balidemaj, C. A. T. Van den Berg, A. L. H. M. W. Van Lier, A. J. Nederveen, L. J. A. Stalpers, H. Crezee and R. F. Remis, "B1-based SAR reconstruction using contrast source inversion-electric properties tomography (CSI-EPT)," *Med. Biol. Eng. Comput.*, Apr. 2016.

[21] P. M. Van den Berg and A. Abubakar, "Contrast source inversion method: state of art," *Progr. Electromagn. Res.*, vol. 34, pp. 189-218, 2001.

[22] R. D. Ryne, "On FFT-based convolutions and correlations, with application to solving Poisson's equation in an open rectangular pipe," arXiv:1111.4971, 2011.

[23] A. Zakaria, C. Gilmore and J. LoVetri, "Finite-element contrast source inversion method for microwave imaging," *Inv. Probl.*, vol. 26, no. 11, 2010.

[24] C. M. Collins, B. Yang, Q. X. Yang and M. B. Smith, "Numerical calculations of the static magnetic field in three-dimensional multi-tissue models of the human head," *Magn. Reson. Imag.*, vol. 20, no. 5, pp. 413-424, Jun. 2002.

[25] A. Bossavit, *Computational electromagnetism*. San Diego, CA: Academic Press, 1998.

[26] R. A. Elliott, *Electromagnetics: history, theory, and applications*. New York, NY: IEEE Computer Society Press, 1993.

[27] D. I. Hoult, "The principle of reciprocity in signal strength calculations—a mathematical guide," *Conc. in Magn. Reson.*, vol. 12, no. 4, pp. 173-187, Mar. 2000.

[28] M. Frigo, and S. G. Johnson, "The Design and Implementation of FFTW3," *Proc. IEEE*, vol. 93, no. 2, pp. 216-231, Feb. 2005.

[29] A. Abubakar, G. Pan, M. Li, L. Zhang, T.M. Habashy, and P.M. van den Berg, "Three-dimensional seismic full-waveform inversion using the finite-difference contrast source inversion method," *Geophysical Prospecting*, vol. 59, no. 5, pp.874-888, Sep. 2011.

[30] J. R. Shewchuk, "Triangle: engineering a 2D quality mesh generator and delaunay triangulator," in *Applied Computational Geometry. Towards Geometric Engineering*, M. C. Lin and D. Manocha, Ed. Berlin: Springer-Verlan, 1996, pp. 203-222.

[31] Gaël Guennebaud and Benoît Jacob and others (2010). Eigen v3. [Online]. Available: http://eigen.tuxfamily.org

[32] A. Christ, W. Kainz, E. G. Hahn, K. Honegger, M. Zefferer, E. Neufeld, W. Rascher, R. Janka, W. Bautz, J. Chen, B. Kiefer, P. Schmitt, H. P. Hollenbach, J. Shen, M. Oberle, D. Szczerba, A. Kam, J. W. Guaq, N. Kuster, "The Virtual Family—development of surface-based anatomical models of two adults and two children for dosimetric simulations," *Phys. Med. Biol.*, vol. 55, no. 2, pp. N23-N38, Jan. 2010.

[33] IT'IS Foundation (2016). Database for thermal and electromagnetic parameters of biological tissues. [Online]. Available: http://www.itis.ethz.ch/database

[34] Guidance for the submission of premarket notifications for magnetic resonance diagnostic devices, US Food and Drug Administration, 1998.

[35] Medical electrical equipment – Part 2-33: Particular requirements for the safety and essential performance of magnetic resonance equipment for medical diagnosis, EN/IEC 60601-2-33, 2010.

[36] G. Tiberi, private communication, Sep. 2016.

[37] P. A. Barrière, J. Idier, J. J. Laurin, and Y. Goussard, "Contrast source inversion method applied to relatively high contrast objects," *Inv. Probl.*, vol. 27, no. 7, Jul. 2011.

[38] A. Abubakar, W. Hu, P. M. van den Berg, and T. M. Habashy, "A finite-difference contrast source inversion method," *Inv. Probl.*, vol. 24, no. 6, 2008.

[39] M. Li, O. Semerci, and A. Abubakar, "A contrast source inversion method in the wavelet domain," *Inv. Probl.*, vol. 29, no. 2, Feb. 2013.

[40] U. Katscher, D. H. Kim, and J. K. Seo, "Recent progress and future challenges in MR electric properties tomography," *Comput. and Math. Meth. in Med.*, vol. 2013, 2013.